Role of Ce^{4+} in the Scintillation Mechanism of Codoped Gd_{3}Ga_{3}Al_{2}O_{12}:Ce

Yuntao Wu, Fang Meng, Qi Li, Merry Koschan, and Charles L. Melcher

1 **The role of Ce^{4+} in scintillation mechanism: Codoped $Gd_3Ga_3Al_2O_{12}$:Ce**

2 Yuntao Wu*[a,b,c], Fang Meng[a,b], Qi Li*[d], Merry Koschan[b], Charles L. Melcher[a,b]

3 [a] *Scintillation Materials Research Center, University of Tennessee, Knoxville, Tennessee 37996, USA*

4 [b] *Department of Materials Science and Engineering, University of Tennessee, Knoxville, Tennessee*
5 *37996, USA*

6 [c] *Shanghai Institute of Ceramics, Chinese Academy of Sciences, Jiading, Shanghai 201899, P.R. China*

7 [d] *Department of Physics, Wake Forest University, Winston-Salem, NC 27109, USA*

8 **Abstract** To control the time response performance of widely used cerium-activated scintillators in

9 cutting-edge medical imaging devices, such as time-of-flight positron emission tomography, a

10 comprehensive understanding of the role of Ce valence states, especially stable Ce^{4+}, in the scintillation

11 mechanism is essential. However, despite some progress made recently, an understanding of the

12 physical processes involving Ce^{4+} is still lacking. The aim of this work is to clarify the role of Ce^{4+} in

13 scintillators by studying Ca^{2+} codoped $Gd_3Ga_3Al_2O_{12}$:Ce (GGAG:Ce). By using a combination of

14 optical absorption spectra and X-ray absorption near edge spectroscopies, the correlation between Ca^{2+}

15 codoping content and Ce^{4+} fraction is seen. The energy level diagrams of Ce^{3+} and Ce^{4+} in the

16 $Gd_3Ga_3Al_2O_{12}$ host have been established by using theoretical and experimental methods, which

17 indicate a higher position of the $5d_1$ state of Ce^{4+} in the forbidden gap in comparison to that of Ce^{3+}.

18 Underlying reasons for the decay time acceleration resulting from Ca^{2+} codoping are revealed, and the

19 physical processes of the Ce^{4+} emission model is proposed and further demonstrated by

20 temperature-dependent radioluminescence spectra under X-ray excitation.

21 **Kew words:** Ce^{4+}, scintillator, codoping, luminescence.

22 Corresponding author email: ywu52@utk.edu, caswyt@hotmail.com (Y.T. Wu), liq9@wfu.edu (Q. Li).
23

I. INTRODCUTION

Positron emission tomography (PET), as a highly sensitive non-invasive medical imaging

technique, is ideally suited for pre-clinical and clinical imaging of cancer biology, which is important to

cancer imaging [1]. Inorganic scintillation crystals, as the key components in PET, are utilized to detect

γ-rays produced by the annihilation of positrons emitted by injected tracers. The ultimate performance

of the PET camera strongly relies on the physical and scintillation properties of the crystals [2]. So far,

the single crystal scintillators for commercial PET cameras are $Bi_4Ge_3O_{12}$ (BGO) [3], Lu_2SiO_5:Ce

(LSO:Ce) [4], and the $Lu_{1.8}Y_{0.2}SiO_5$:Ce (LYSO:Ce) [5]. Significant improvements have made it

possible to add the technology of time-of-flight (TOF) to improve the image quality of PET [6]. Among

the single crystals used for PET applications, LSO:Ce is the best candidate for TOF-PET application

because of the key parameter of short decay time, e.g. 40 ns for LSO:Ce [4]. One requirement for TOF

is the best possible coincidence time resolution (CTR), the figure of merit of which should be 200 ps or

better [7]. Since excellent timing resolution can best be achieved on a scintillator with faster decay time

and higher light yield [8], a divalent ion codoping strategy was applied over the past six years to

improve the time response characteristics in trivalent-cation based oxide scintillators such as

LSO:Ce,Ca, [9] LYSO:Ce,Ca/Mg [10], and $Lu_3Al_5O_{12}$:Ce,Mg (LuAG:Ce,Mg) [11,12] without

sacrificing (or even enhancing) the light yield when a low codoping concentration of 0.1 at% was used.

Compared with a CTR of 190 ps for LSO:Ce, an even better CTR of 170 ps can be measured on a 0.4

at% Ca codoped LSO:Ce single crystal under the same conditions [7], but with relatively lower light

yield. Thus, understanding of the fundamental physical processes causing the acceleration of decay

kinetics by divalent codoping is essential for designing other promising candidates for TOF-PET

application.

There are some hypotheses in the literature for the mechanism of decay time shortening as a result

of codoping. In LSO:Ce,Ca, a proposed cause was the suppression of the slower emission from the

6-oxygen coordinated Ce2 sites and improved chances for migrating charge carriers to be captured by

the faster 7-oxygen coordinated Ce1 sites [13]. It has also been ascribed to the reduction of traps acting

to slow the scintillation process [14]. Recently, a model of Ce^{4+} ions as an intermediate state in the

process leading to a Ce^{3+} excited state was used to explain the decay time acceleration of LYSO:Ce

single crystals by Ca^{2+} or Mg^{2+} codoping [10]. Nevertheless, without solid evidence such as

observation of $(Ce^{3+})^*$ excitation emission from a scintillator material in which Ce^{4+} has dominating

54 concentration over Ce^{3+}, the Ce^{4+} emission model is still not firmly proved.

55   The $Gd_3Ga_3Al_2O_{12}$:Ce (GGAG:Ce) single crystal scintillator was developed as an improvement of

56 the LuAG:Ce scintillator, based on band-gap engineering [15,16] and cerium valence instability [17] by

57 a Ga^{3+} admixture, and energy level positioning by a Gd^{3+} admixture [18,19]. It shows very high light

58 yield of up to 50,000 photons/MeV, which exceeds by 30-40% the light yield value of the best

59 LYSO:Ce scintillators ever reported [20]. A 2 inch diameter GGAG:Ce single crystal was successfully

60 grown at the Furukawa Co. Ltd. in 2012, which was expected to be a promising candidate for use in

61 PET [21]. However, its main decay component of 88 ns [21], a relatively slow time response compared

62 with LSO:Ce, might be a bottleneck that hinders its application. Our recent work has shown that the

63 decay kinetics of GGAG:Ce can be accelerated by codoping with Ca^{2+} ions, though at the expense of

64 light yield [22]. At certain Ca^{2+} codoping concentration, such as 0.1 at%, the scintillation decay time

65 can be shortened to about 46 ns with a light yield of about 40,000 photons/MeV [23], which may pave

66 the way to its PET and TOF-PET applications.

67   Clarifying the role of a Ca^{2+} codopant in $Gd_3Ga_3Al_2O_{12}$:Ce scintillation kinetics with an eye

68 toward enabling design of advanced compositions for Ce^{3+} activated PET and TOF-PET applications

69 served as a motivation for this work. Here we report the correlation between Ca^{2+} codoping

70 concentration and the Ce^{3+}/Ce^{4+} ratio as determined by optical absorption spectra and X-ray absorption

71 near edge spectroscopy (XANES). By varying the Ca^{2+} codoping concentration, a sample almost

72 completely activated by Ce^{4+} was identified. The related energy level diagram of Ce^{3+} and Ce^{4+} in the

73 GGAG:Ce host was constructed by using the three-parameter experimental method [24] and the

74 DFT+G_0W_0 theoretical calculation method. The higher position of the lowest $5d_1$ excited state of Ce^{4+}

75 in the forbidden gap in comparison to that of Ce^{3+} was confirmed. Furthermore, a Ce^{4+} emission model

76 is presented and corroborated by temperature-dependent radioluminescence spectra under X-ray

77 excitation. Based on these results, the fundamental origins of the shorter decay time resulting from Ca^{2+}

78 codoping in GGAG:Ce is addressed and compared to the cases of Ca^{2+} or Mg^{2+} codoped LSO:Ce,

79 LYSO:Ce and LuAG:Ce. Experiments on B^{3+} and Ba^{2+} codoped GGAG:Ce single crystals were also

80 done for comparison.

81

82 **II. EXPERIMENTAL AND THEORETICAL METHODS**

83   Seven GGAG crystals were grown via the Czochralski method. The compositions are given in

84   TABLE I. All crystals were grown in inductively heated ∅ 60 mm × 60 mm iridium crucibles in a

85   Cyberstar Oxypuller 05-03 Czochralski growth station. Three percent excess Ga was added to an

86   otherwise stoichiometric melt composition in order to compensate for its volatilization loss from the

87   melt. In all cases, the dopant and codopant concentrations given refer to the initial starting melt and

88   calculations were based on the assumption that the dopants substituted for Gd based on atomic size

89   matching. Note that the dopant concentrations in the finished boules will differ from that in the melt

90   due to segregation at the solid-liquid interface. The growth atmosphere was flowing nitrogen with a

91   small fraction of a percent oxygen.

92   **TABLE I.** The concentration of activator and codopants in GGAG melt, the concentration given are
93   respect to Gd.

Compositions	Ce concentration (at%)	Codopant concentration (at%)
GGAG:Ce	0.2	-
GGAG:Ce,Ca	0.2	0.1
	0.2	0.2
	0.2	0.4
GGAG:Ce,Ba	0.2	0.2
GGAG:Ce,B	0.2	0.2

94

95   Optical absorption spectra were measured with a Varian Cary 5000 UV–VIS– NIR

96   spectrophotometer in the 200-800 nm range. Photoluminescence (PL) emission and excitation

97   spectra were measured with a HORIBA Jobin Yvon Fluorolog-3 spectrofluorometer. The

98   excitation light passed through an excitation monochromator with a 1 nm bandpass to ensure

99   monochromaticity. Similarly, the emission monochromator was set at a 1 nm bandpass to select

100   emission light of a specific wavelength. A 450W continuous xenon lamp was used as the

101   excitation source in emission and excitation spectra.

102   XANES spectra of codoped GGAG:Ce single crystals were recorded at BL14W1, a

103   wiggler-based beamline in the Shanghai Synchrotron Radiation Facility (SSRF).

104   Room-temperature measurements were made at the Ce L_{III}-edge (5723 eV), in the fluorescence

105   mode due to the low cerium content, using a Si (111) double crystal monochromator. The

106   XANES spectra were recorded in two regions: (1) from 5700 to 5720 eV (pre-edge) every 0.5

107   eV with 5 s accumulation time per point; (2) from 5720 to 5780 eV (XANES), every 0.5 eV

108   with 8 s accumulation time per point. The powders were evenly coated on transparent tape for

109   measurements. The XANES spectra of Ce^{4+} and Ce^{3+} standard samples were recorded at the

110   XAFS station of Beijing Synchrotron Radiation Facility (BSRF) and the specific measurement

111   description can be found in Ref. 25. All spectra were normalized in the same way using the

112   Athena software [26].

113   For temperature-dependent radioluminescence spectra, a sample was mounted on a cold

114   finger of the cryostat. The pressure was reduced to 12 mTorr and the sample was measured

115   from 500 K to 40 K to avoid interference from thermoluminescence when irradiated by an

116   X-ray generator (X-ray Model; CMX003) at 35 kV and 0.1 mA.

117   The absolute light yield measurement was recorded by using a pulse processing chain

118   consisting of an Hamamatsu R2059 photomultiplier tube (PMT) operated at -1500 V_{bias}, an

119   Ortec 672 Amp, a Canberra model 2005 pre-Amp and a Tukan 8k multi-channel analyser. The

120   PMT was directly coupled to each sample using mineral oil, and a PTFE-lined dome-shaped

121   reflector with a 50 mm diameter was used to maximize the collection of light. The

122   photoelectron yield of the samples was calculated by using the single photoelectron peak

123   method. Measurements on the samples were made at a gain of 5 with 2 µs shaping time to

124   provide full light integration. The sample was measured for 20 min during its irradiation with a

125   15 µCi ^{137}Cs source at a distance of about 20 cm. The reproducibility of light yield is ±5%.

126   Electronic structure calculations of bulk GGAG crystals were carried out using the Vienna

127   Ab-initio Simulation Package (VASP) [27,28] with projector augmented wave (PAW)

128   pseudopotentials and generalized gradient approximation exchange-correlation functionals

129   parametrized by Perdew-Burke-Ernzerhof (PBE) [29]. DFT+U on-site potentials [30] were

130   included for Gd-4f orbitals with $\underline{U}_{eff}$ = 6eV [31]. Traditional DFT underestimates band seriously

131   in general and hence is not able to make accurate predictions for the relative energy levels [32].

132   To solve this problem, we employed hybrid functional PBE0 [33] and GW approximation [34]

133   to determine the band gaps and the positions of Ce^{3+} $4f$ and $5d$ levels. The crystal structure of

134   the $RE_3Al_5O_{12}$ (RE = rare earth) prototype is body centered cubic of space group Ia-3d with 160

135   (80) atoms in the cubic conventional (primitive) cell [35]. Experimental evidence shows that the

136   substitutional Ga_{Al} can occupy both octahedral (16a) and tetrahedral (24d) sites. We performed

137   calculations on both "ordered" GGAG in which the Ga atoms only occupy 24d sites and

138   160-atom special quasi-random structure (SQS) [36] with fixed Ga/Al ratio (1:1 on 16a and 2:1

139   on 24d) [37] to simulate the complex. The Ce levels are simulated by one Ce_{Gd} impurity in the

140   160 atom cell. GW approximation was applied on top of GGA+U wavefunctions. The Ce^{4+}

141   impurity is simulated by removing one electron from the cell, and a negative background

142   electron density is added to the system. The kinetic cut-off energy was 500 eV. Calculations

143   sampling the gamma-point only were performed but the calculations converge within 1

144   meV/atom. A self-consistency convergence tolerance of 1×10^{-6} eV was used for all calculations

145   and the structures were relaxed until all the force components became less than the 0.01 eV/Å.

146   The volumes of the lattices were relaxed with the shape of the cells fixed as cubic.

147
148   **III. RESULTS AND DISCUSSION**

149   **A. Phenomenon: scintillation decay time shortening after Ca^{2+} codoping**

150   Scintillation decay curves at room temperature are shown in FIG. 1 for GGAG:Ce and

151   Ca^{2+}-codoped GGAG:Ce single crystals. All decay curves are approximated by two exponentials,

152   corresponding to the prompt and delayed radiative recombination at the Ce^{3+} centers [12]. The peak at

153   370 ns is thought to be an experimental artifact. The decay components determined from a fit of the

154   experimental data to a two exponential function are listed in TABLE II for all four samples. The most

155   important observation is the continuous shortening with increasing Ca^{2+} concentration of both the

156   prompt and delayed radiative recombination components, similar to the cases of Ca^{2+}-codopd LSO:Ce

157   single crystal [9], Mg^{2+}-codoped LuAG:Ce optical ceramic [11] and single crystal [12]. Specifically,

158   the fast component decreases from 50 ns for uncodoped sample to 22 ns for 0.4 at% Ca codoped

159   sample, and the slow component in the 0.4 at% Ca codoped sample is an order of magnitude faster than

160   the non-codoped sample. However, the decay components in GGAG with Ba^{2+} and B^{3+} codoping

161   become slower than in non-codoped samples [22].
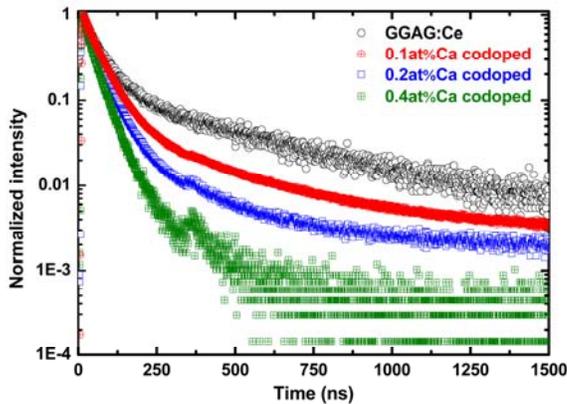
162

163   **FIG. 1 Scintillation decay profiles of GGAG:Ce and Ca^{2+}-codoped GGAG:Ce single**
164   **crystals under ^{137}Cs γ-ray source excitation at room temperature.**

166 **TABLE II.** Scintillation decay time components of GGAG:Ce doped with different Ca^{2+} concentration
167 and the corresponding percentage of the total scintillation output.

Compositions	Decay components	
	Fast (ns)	Slow (ns)
GGAG:Ce	50 (50%)	372 (50%)
GGAG:Ce,0.1at% Ca	45 (73%)	226 (27%)
GGAG:Ce,0.2at% Ca	40 (78%)	137 (22%)
GGAG:Ce,0.4at% Ca	27 (59%)	59 (41%)

168

169 **B. Evidence of increased Ce^{4+} percentage**

170   Optical absorption spectra of Ca^{2+} codoped GGAG:Ce single crystals are plotted in FIG. 2(a) as

171 well as the spectra for B^{3+} and Ba^{2+} codoped GGAG:Ce. The $4f \rightarrow 5d_{1,2}$ transitions of Ce^{3+} centered at

172 340 and 438 nm, and the Gd^{3+} $4f \rightarrow 4f$ transition $^8S_{7/2} \rightarrow ^6I_{3/2}$ at 275 nm [38] can be observed in

173 GGAG:Ce. The B^{3+} or Ba^{2+} codoped samples show similar absorption features. Ca^{2+} codoping

174 significantly changes the absorption features. The intensity of the $4f\text{-}5d_1$ absorption band shows a

175 decreasing trend after Ca^{2+} codoping, and almost vanishes when the Ca^{2+} codoping concentration

176 reaches 0.4 at%. It implies that the fraction of cerium that is in trivalent form is negligible. Furthermore,

177 the absorbance of Ca^{2+} codoped GGAG:Ce increases in the region of 200-370 nm compared to

178 GGAG:Ce. A similar broad absorption band peaking at around 260 nm has been ascribed to the charge

179 transfer (CT) transition from the O^{2-} levels to the Ce^{3+} ground state in Mg^{2+}-codoped LuAG:Ce [11]

180 and Ca^{2+}-codoped LYSO:Ce [10,39]. The remarkable enhancement of CT absorption intensity with

181 increasing Ca^{2+} concentration indicates an increase in the stable Ce^{4+} fraction, which is consistent with

182 the decreasing intensity of the $4f \rightarrow 5d_1$ absorption of stable Ce^{3+}. The driving force of the formation of

183 Ce^{4+} is achievement of the charge compensation required when divalent Ca ions locate at trivalent Gd

184 sites. It should be noted that divalent Ba^{2+} codoping does not show the same effect as Ca^{2+} codoping.

185 We assume that this is due to a very low concentration of Ba^{2+} in the lattice due to its much larger ionic

186 radius, which is about 142 pm for the octa-coordinated site. In comparison, Gd^{3+} is 105.3 pm and Ca^{2+}

187 is 112 pm [40].

188   Excitation spectra are much more sensitive to a trace presence of the emission center than are

189 absorption spectra. Consequently, one can detect the center existence via emission spectroscopy, even

190 when it is practically invisible in absorption. To determine if Ce^{3+} is present in a 0.4 at% Ca^{2+} codoped

191 GGAG:Ce sample, its photoluminescence excitation and emission were measured; the spectra are

192 shown in FIG.2(b). Under identical measurement conditions we observe that the $Ce^{3+} 4f \rightarrow 5d_{1,2}$

193   excitation peaks at 340 nm and 438 nm and the *5d→4f* emission peak at 550 nm are very weak in 0.4 at%

194   Ca^{2+} codoped GGAG compared with GGAG:Ce, and the integrated PL intensity in the Ca^{2+} codoped

195   sample is at least one order of magnitude lower than that of non-codoped GGAG:Ce. This indicates that

196   the Ce^{3+} is at a trace level in the 0.4 at% Ca^{2+} codoped sample. It is worth mentioning that when grown

197   under the same conditions, the 0.4 at% Ca codoped GGAG:Ce single crystal is a red-brown color,

198   which is completely different from the yellow color of GGAG:Ce single crystals codoped with other

199   Ca^{2+} concentrations (see FIG.2(c)).
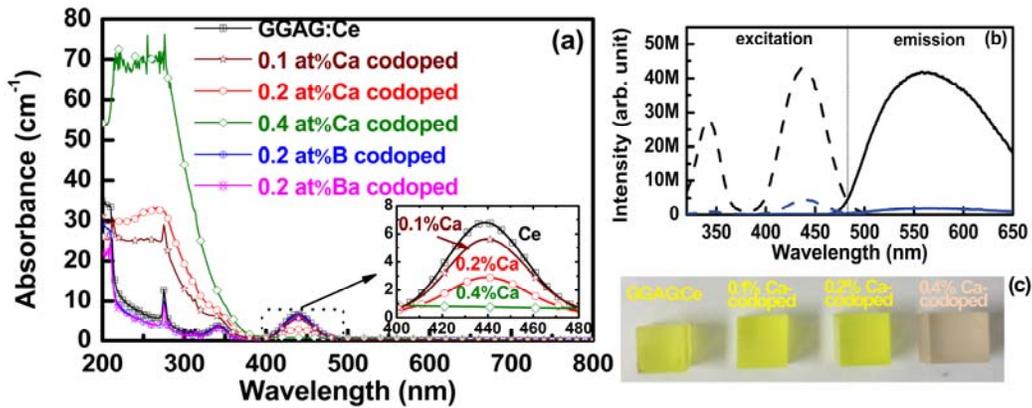
200

201   **FIG. 2** (a) Optical absorption spectra of GGAG:Ce, GGAG:Ce,B, GGAG:Ce,Ba, and GGAG:Ce,Ca
202   single crystals. The inset is a close-up view for the Ca^{2+} codoped GGAG:Ce single crystals in the
203   400-480 nm range; (b) Photoluminescence excitation (λ_{em}=550 nm) and emission (λ_{ex}=345 nm) spectra
204   of GGAG:Ce (black curves) and 0.4 at% Ca^{2+}-codoped GGAG:Ce (blue curves) single crystals; (c) the
205   Ca^{2+} codoped GGAG:Ce single crystal samples.
206
207   In order to directly verify the variation of the cerium valence state before and after codoping,

208   X-ray absorption near edge spectroscopy (XANES) is utilized. XANES at the Ce L_{III}-edge of

209   GGAG:Ce and 0.4 at% Ca^{2+} codoped GGAG:Ce are presented in FIG. 3(a). XANES of B^{3+} and Ba^{2+}

210   codoped complexes are also shown. The XANES spectra of Ce^{4+} and Ce^{3+} comparison samples

211   recorded at the Ce L_{III}-edge are shown in FIG. 3(b). By comparing the peak shape and the edge position

212   with the reference CeO_2 and CeF_3 samples, the valence states of cerium in these GGAG samples can be

213   determined. Peak A is the Ce^{4+} peak with the final state *$2p4f^{0}5d^{1}$* and peak B is also a Ce^{4+} peak with

214   the final state of *$2p4f^{1}5d^{1}$*. Peak C at about 5723 eV is a Ce^{3+} peak, which is associated with the *$2p4f^{1}5d$*

215   dipole allowed transition [41]. The XANES data from the GGAG:Ce single crystal indicates that it is a

216   mixture of about 50% Ce^{3+} and 50% Ce^{4+}, as can be seen by comparison with the mixed reference

217   sample. This is quite different than the pure Ce^{3+} results previously reported for the case of LSO:Ce

218   single crystals [4,42], even though the LSO and GGAG samples were grown in essentially the same

219   growth atmosphere. The XANES data from the 0.4 at% Ca^{2+}-codoped GGAG:Ce sample shows typical

8

220   Ce^{4+} features. Due to the signal-to-noise limitation, the $I(Ce^{3+})/(I(Ce^{3+})+I(Ce^{4+}))$ ratio cannot be derived

221   by the linear combination fitting method. However, when considering the area under the *4f-5d₁*

222   transition of Ce^{3+} in the Ca-free and 0.4 at% Ca^{2+}-codoped samples (see FIG. 2(b)), the Ce^{3+} fraction in

223   0.4 at% Ca^{2+}-codoped sample can be estimated to be approximately 4%. Thus, the practical Ce^{3+}

224   concentration the in 0.4 at% Ca^{2+} codoped GGAG crystal is roughly estimated to be less than 6 ppmw,

225   given an initial cerium concentration of 458 ppmw and an effective distribution coefficient of 0.322 for

226   cerium ions in GGAG [21], and a Ce^{3+} ratio of 4%. So far, only SiO_2:0.01 mol% Ce sintered in an

227   oxidizing atmosphere has been reported to contain 100% of Ce^{4+} as measured via absorption spectra

228   [43]. Examination of the shoulder corresponding to peak A for B^{3+} or Ba^{2+} codoped samples reveals an

229   apparent reduction in absorption intensity, consistent with decreasing Ce^{4+} content. This phenomenon is

230   in good agreement with the changes in the CT absorption when compared with the GGAG:Ce.

231   Therefore, the phenomena described above imply a close correlation between scintillation response

232   acceleration and tetravalent cerium concentration increase.
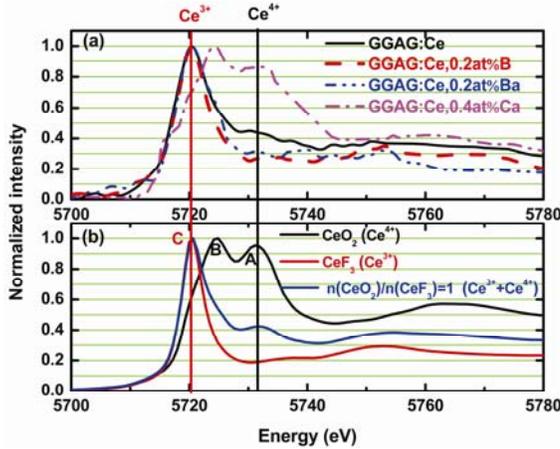
233

234   **FIG. 3** (a) Ce L_{III}-edge XANES spectra of GGAG:Ce, GGAG:Ce,0.2 at% B^{3+}, GGAG:Ce, 0.2 at%
235   Ba^{2+}, and GGAG:Ce,0.4 at% Ca^{2+} single crystals; (b) The XANES spectra of the Ce^{4+} and Ce^{3+}
236   standard samples recorded at Ce L_{III}-edge are used as references.
237

238   **C. Energy level diagram construction**

239   To shed light on the luminescence behaviors, we constructed the energy level diagrams of Ce^{3+}

240   and Ce^{4+} in GGAG by the three-parameter method based on E_{4f-5d1} and E_{CT} for Ce^{4+}, and E_{4f-5d} and E_{cd}

241   for Ce^{3+}, and E_g. We present the results from first principles calculations. The calculated lattice

242   constants and bandgaps for $Gd_3Al_5O_{12}$ (GAG), ordered GGAG, and SQS-GGAG are listed in TABLE

243   III. Experimental results are also listed for comparison. Both functionals overestimate the lattice

244   constants. PBE0 predicts smaller deviation of the lattice constant from experiment. The SQS structure

245   is predicted to have smaller lattice constants compared to ordered GGAG. Similar results were obtained

246   in Ref. [45]. Accordingly, higher bandgaps are predicted for SQS-GGAG. The bandgap is significantly

247   reduced (~ 0.7 eV from PBE0) by Ga doping in the original GAG crystals, consistent with the

248   "bandgap engineering" mechanism in Ref. 16. Based on the exciton energy ($E_{exciton}$) for GGAG

249   reported in Ref. [44] and the rule of thumb E_g=1.08$\times E_{exciton}$ [44]), E_g is calculated to be 6.8 eV as

250   listed in TABLE III. Use of the PBE0 functional produces a bandgap (6.4 eV) matching experimental

251   prediction closely.

252   **TABLE III.** Calculated lattice constants (a) and bandgaps (E_g) of GAG, ordered GGAG and
253   SQS-GGAG using different functionals.

	GAG		GGAG-ordered		GGAG-SQS	
	a (Å)	E_g (eV)	a (Å)	E_g (eV)	a (Å)	E_g (eV)
GGA+U	12.20	3.96	12.41	3.62	12.40	3.64
PBE0	12.11	7.16	12.30	6.35	12.28	6.40
Expt.	12.11 [a]	7.07 [b]	-	-	12.27 [c]	~6.80

254   [a] Derived from Powder Diffraction File for $Gd_3Al_5O_{12}$ (PDF 73-1371);
255   [b] Derived from Ref. 44;
256   [c] See supplemental material I.

257
258   The partial density of states (PDOS) of SQS-GGAG calculated by GGA+U and PBE0 is shown in

259   FIG. 4. The plot shows the PDOS for two different spin states indicated by positive and negative values.

260   The top of the valance band consists mainly of O 2p states and the conduction band minimum (CBM)

261   consists of Ga 5s states. Based on our PBE0 results, there is a significant splitting between the two spin

262   states of the Gd 4f orbitals. The first spin state accommodates all 7 4f electrons of Gd and is 3.5 eV

263   below the VBM. The other spin state of Gd 4f orbitals are unoccupied, lying at 2.5 eV above CBM.

264   The CBM Ga 5s states calculated by the PBE0 functional shown in FIG. 3 are more localized compared

265   to GGA+U results, however, it is a nonphysical result introduced by insufficient K-mesh sampling. The

266   PDOS results from the PBE0 functional were constructed by using a 2×2×2 K-mesh because of

267   exceedingly high computational complexity when using more refined K-mesh sampling with PBE0

268   functional. We performed DFT+G_0W_0 calculations to make the most accurate predictions for the

269   energy levels. The positions of the lowest 4f and 5d levels of Ce relative to VBM/CBM for Ce^{3+} and

270   Ce^{4+} are shown in FIG. 5(a). The band gap calculated using G_0W_0 is 6.63 eV, which is even closer to

271   the experimental evaluation compared to PBE0 hybrid functional results (6.40 eV). Both of the lowest

272   4f and 5d levels of Ce lie inside the forbidden gap of the host crystal. The 4f→5d_1 transition energy is

273   quite close, being 2.68 eV and 2.65 eV respectively in Ce^{3+} and Ce^{4+}. A previous ab-initio calculation

274   based on quantum cluster approaches predicted the 4f→5d transition of 23927 cm^{-1} (2.97 eV) for

275   Ce_Y,Ga_{Al}^{oct}:YAG systems [46]. By localizing a hole at the Ce_{Gd} site, the lowest Ce *4f* level becomes

276   unoccupied and the *4f*-VBM gap increased from 3.13 eV to 3.60 eV. Correspondingly, the lowest 5d

277   level in Ce^{4+} is pushed up toward the CBM, leaving a *5d*-CBM gap of 0.38 eV compared to 0.82 eV in

278   Ce^{3+}. Based on the calculation results, the theoretical energy level diagrams of Ce^{3+} and Ce^{4+} are

279   constructed and plotted in FIG. 5(a).

280   As shown in FIG. 2(a), E_{CT} seems to be within 3.35-3.18 eV (370-390 nm). However, the accurate

281   estimation of the onset of CT absorption of Ce^{4+} (E_{CT}) is influenced by the existence of an additional

282   excitation band between 3.54 and 3.26 eV (350-380 nm) in Ca^{2+} codoped GGAG:Ce [23]. Based on its

283   fast PL decay time of 3.6 ns and a small Stokes shift of 0.4 eV, along with its correlation with

284   atmosphere annealing, the absorption band is related to F^+ centers (positively charged oxygen vacancies)

285   [23], which was also shown in La^{3+} doped LuAG single crystals [47] and undoped LuAG single

286   crystals [48]. By analysis of the results of annealing Ca^{2+} codoped GGAG:Ce in air atmosphere, e.g.

287   0.2 at% Ca codoped GGAG, the influence of the absorption band associated with F^+ center can be ruled

288   out and the authentic onset of CT absorption of Ce^{4+} can be estimated to be 323 nm (3.84 eV) [22],

289   which shifts to the higher energy side in comparison to the E_{CT} of 3.65 eV (340 nm) for LuAG:Ce,Mg

290   [11] and 3.65-3.54 eV (340-350 nm) for LYSO:Ce,Ca/Mg [10,39]. E_{cd} for Ce^{3+}, the energy separation

291   between the *5d$_1$* state of Ce^{3+} and the conduction band, was reported to be 0.42 eV [22]. We recall that

292   the $E_{4f\text{-}5d1}$ for Ce^{3+} is 2.83 eV (438 nm) (see FIG. 2). Under the assumption of comparable Stokes shift

293   the $E_{4f\text{-}5d1}$ value for Ce^{4+} is assumed to be the same as that of Ce^{3+} owing to identical radioluminescence

294   emissions (See FIG.7) [10]. On the basis of the above optical parameters, the experimental energy level

295   diagrams of Ce^{3+} and Ce^{4+} in GGAG host were constructed and plotted in FIG. 5(b). The deviation

296   between E_{CT} and E_{Vf} (the energy separation between the top of VB and the *4f* ground state of Ce^{3+}) is

297   within 0.5 eV, which suggests the Coulomb interaction between the electron transferred to Ce^{3+} ions

298   and the hole kept at O^{2-} ions does compensate for the relaxation energy of charge transfer state [24]. It

299   is worth noticing that these energy level positions are in good agreement with the theoretical

300   calculation results, although slight differences in their absolute values exist. It is apparent that in both

301   diagrams the *4f→5d$_1$* transition energies are equal for Ce^{3+} and Ce^{4+}, and the Ce^{4+} *5d$_1$* state locates in a

302   higher position in the forbidden gap in comparison to that of Ce^{3+}.

303
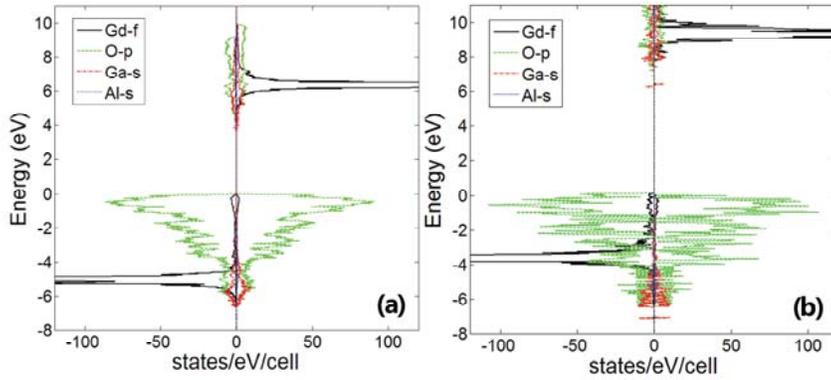
FIG. 4 Calculated partial density of states of 160 atom SQS of GGAG using GGA+U (a) and PBE0 (b)
functionals. Positive/Negative values represent two different spin states.

306

307
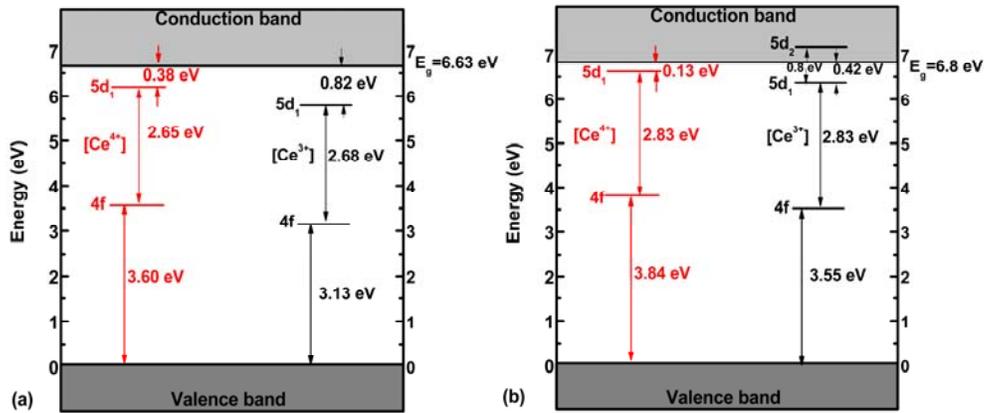
FIG. 5 Schematic energy level diagrams of Ce^{3+} and Ce^{4+} centers in the GGAG:Ce host: (a) theory
(DFT+G_0W_0); (b) experiment (three-parameter method).

310

D. Modeling Ce^{4+} emission

To prove that the scintillation occurs from Ce^{4+}, pulse height measurements under [137]Cs

gamma-ray source excitation were made of both of 0.4 at% Ca^{2+} codoped GGAG:Ce, a sample

containing negligible Ce^{3+}, and non-codoped GGAG:Ce; results are shown in FIG. 6. Using the data

from the radioluminescence spectra, the emission weighted quantum efficiency (EWQE) of the R2059

PMT was found to be 10% for both samples. The light yield of the 0.4 at% Ca^{2+} codoped sample is

estimated to be 14,800±740 photons/MeV, about one third of that in GGAG:Ce (44,600±2230

photons/MeV). In general, the featured photoluminescence excitation (or absorption) and emission

bands of Ce^{3+} can be observed even though its content is at trace levels [49,50], but it is not sufficient

to account for all of the measured photons. Therefore, Ce^{4+} ions must play a vital role in the

scintillation emission. Sr_2CeO_4 is one of the rare materials in which Ce^{4+} luminescence has been

reported, and in this material the emission was assigned to a ligand-to-metal CT transition of Ce^{4+}

12

323 [51,52]. However, as for 0.4 at% Ca^{2+} codoped GGAG:Ce, an almost pure Ce^{4+} sample, Ce^{3+} emission

324 peaks observed under X-ray excitation (see FIG. 7) and a fast decay time in the ns scale under γ-ray

325 excitation (see FIG. 1) indicate that the Ce^{4+} emission model cannot be assigned to a CT emission, but

326 another physical process through an intermediate Ce^{3+} state. Rotman et al. [53] reported that at high

327 Ca^{2+} concentration codoping in garnets the Ce^{3+} centers completely converted into stable Ce^{4+}, but did

328 show typical Ce^{3+} luminescence under accelerated electron excitation in cathodoluminescence spectra.

329 It was explained by an immediate capture of electrons from the conduction band (CB) by stable Ce^{4+}

330 centers which give rise to the excited Ce^{3+} centers and their typical emission afterwards. Similar

331 models have been recently proposed in silicate and garnet scintillators [10,11].
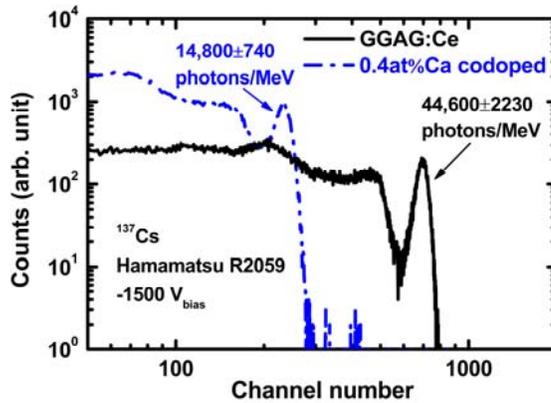
333 **FIG. 6** Pulse height spectra of 662 keV γ-ray detected in GGAG:Ce and 0.4 at% Ca^{2+} codoped
334 GGAG:Ce single crystals obtained with a Hamamatsu R2059 PMT.
335

336 Since for Ce^{3+} thermal ionization to the conduction band is negligible around room temperature

337 (its onset is indicated at 310 K in [19]), a difference is expected with Ce^{4+} due to its higher $5d_1$ position

338 in the forbidden gap. In order to further corroborate the applicability of the physical processes of Ce^{4+}

339 emission, the temperature-dependent radioluminescence spectra of GGAG:Ce with approximate 50%

340 Ce^{4+}, and 0.4 at% Ca^{2+} codoped GGAG:Ce with almost pure Ce^{4+} were acquired, as plotted in FIG. 7(a)

341 and (b). The measurements were recorded from 500 K to 40 K to avoid interference from

342 thermoluminescence [54]. The Ce^{3+} emission was lower at higher temperatures in both cases, although

343 to differing degrees. The integrated intensities derived from X-ray radioluminescence spectra in the

344 region from 450 to 800 nm as a function of temperature are plotted in FIG. 7(c). The quenching of the

345 0.4 at% Ca codoped sample starts at a lower temperature than that of GGAG:Ce, decreasing by 31%

346 over the 300 K to 40 K range, in comparison to a 6% decrease over the same range for GGAG:Ce. This

347 is in good agreement with the a similar measurement reported by Blahuta et al for LYSO:Ce and

13

348   Ca^{2+}-codoped LYSO:Ce [10]. The solid curve shown in FIG. 7(c) represents a model calculation used

349   to describe thermal quenching of luminescence. The measured steady-state integrated intensity $I(T)$ can

350   be expressed as:

351           $$I(T) = \frac{I_0}{1 + \Gamma_{nr}/\Gamma_r \exp\left(-\Delta E/kT\right)} \qquad (1)$$

352   where $I(T)$ is the scintillation emission intensity at temperature T, I_0 the scintillation emission intensity

353   at T=0, and Γ_{nr} and Γ_r are the non-radiative and the radiative transition probability. ΔE is the activation

354   energy related to the ionization and/or quenching process and k the Boltzmann constant. From a fit to

355   Eq. (1) values of ΔE = 296±27 meV for GGAG:Ce and ΔE = 206±7 meV for 0.4 at% Ca^{2+} codoped

356   GGAG:Ce were obtained. This is consistent with the concept that the $5d_1$ position of Ce^{4+} is higher

357   than the $5d_1$ position of Ce^{3+} in the GGAG host and both the stable Ce^{3+} and Ce^{4+} ions serve as

358   luminescence centers in the GGAG host, providing the same spectra under ionizing radiation. It is

359   worth noting that these two activation energies could not be regarded as the ΔE for Ce^{3+} and Ce^{4+},

360   because both Ce^{3+} and Ce^{4+} in these two samples participate in the scintillation process under X-ray

361   irradiation. In other words, the ΔE = 296±27 meV for GGAG:Ce should be underestimated for Ce^{3+},

362   and ΔE = 206±7 meV for 0.4 at% Ca^{2+} codoped GGAG:Ce should be overestimated for Ce^{4+}. In fact,

363   these two values are indeed between 0.42 eV for Ce^{3+} derived from the temperature dependent

364   photoluminescence decays (in which only Ce^{3+} ions participate) and the 0.13 eV for Ce^{4+} obtained from

365   the three-parameter method.

366
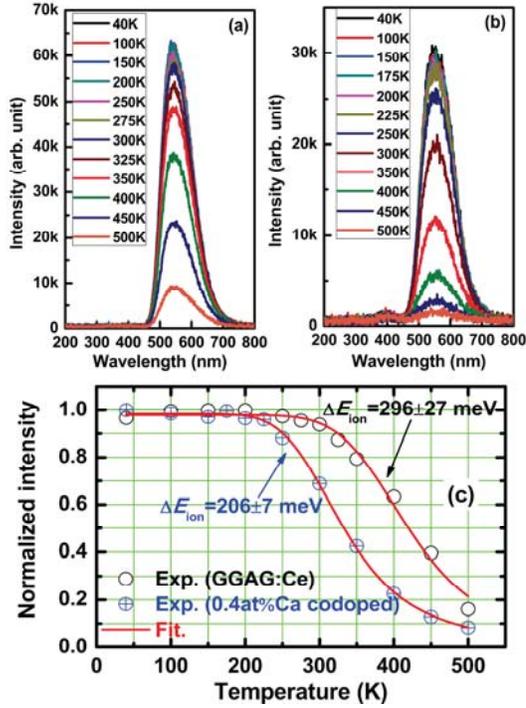
FIG. 7 Temperature-dependent X-ray radioluminescence spectra of GGAG:Ce (a) and 0.4 at% Ca^{2+} codoped GGAG:Ce (b). Their intensity variation as a function of temperature is shown in (c), and the red solid lines are fit following Eq. (1).

According to the physical processes of Ce^{3+} luminescence in scintillators [55], the scintillation process involving a stable Ce^{3+} center in the GGAG host should be creation of initial e-h pairs under ionizing irradiation, then a continuous process of capturing a hole from VB, then capturing an electron from CB, and finally radiative de-excitation followed by photon emission at around 550 nm:

$$Ce^{3+} + h^+ \rightarrow Ce^{4+} \qquad (2)$$

$$Ce^{4+} + e^- \rightarrow (Ce^{3+})^* \qquad (3)$$

$$(Ce^{3+})^* \rightarrow Ce^{3+} + h\nu \qquad (4)$$
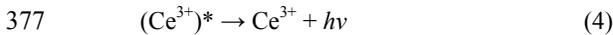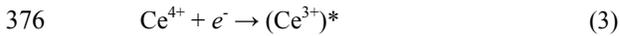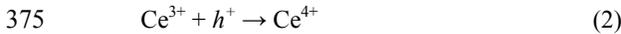
where h^+, e^-, $(Ce^{3+})^*$, and $h\nu$ represent an electron in CB, a hole in VB, an excited Ce^{3+} ion, and the emitted photon, respectively. It is apparent that in these three processes, the Ce^{4+} acts as an intermediate state. Then based on the evidence and analysis of Ce^{4+} emission in GGAG:Ce,Ca above, a schematic diagram of the role of stable Ce^{4+} in scintillation mechanism in GGAG:Ce was developed, as shown in FIG. 8. After irradiation under X-ray or γ-ray, free charge carriers (e-h pairs) are produced in the CB and VB (step 1); a stable Ce^{4+} ion then captures an excited electron from the CB in the empty $5d$ energy levels and the formation of an excited $(Ce^{3+})^*$ center occurs (step 2); the Ce^{3+} emission occurs by radiative de-excitation that leaves the center in the ground state of Ce^{3+} (step 3); stable Ce^{4+}

15

386   is re-created by a hole capture from the valence band or a nearby hole trap (step 4). According to Ref.

387   52, where Ca^{2+} was introduced into garnet system, the VB hole can be trapped at neighboring oxygen

388   ligands so that the Ce^{3+} center in the ground state (after step (3)) can thus trap a hole localized nearby

389   the Ca^{2+} ion or a hole from VB .

390   The underlying reasons for decay time shortening by Ca^{2+} codoping in GGAG:Ce could be related

391   to two factors: (i) a much faster emission based on stable Ce^{4+}, which is made possible by bypassing

392   the first step of the stable Ce^{3+} scintillation mechanism under ionization irradiation, i.e. capturing a hole

393   from VB, and a faster radiative de-excitation of the electron captured at the $5d_1$ state of Ce^{4+} because its

394   E_{cd} is narrower than that of stable Ce^{3+}; (ii) a more efficient energy migration of free charge carriers to

395   activators due to the reduction in the number of shallow traps [22]. The deterioration of light yield after

396   Ca^{2+} codoping could be related to two factors: (i) the negative consequence of the smaller E_{cd} of Ce^{4+}

397   and (ii) formation of deep traps corresponding to the TL peaks over 300 K [22].

398
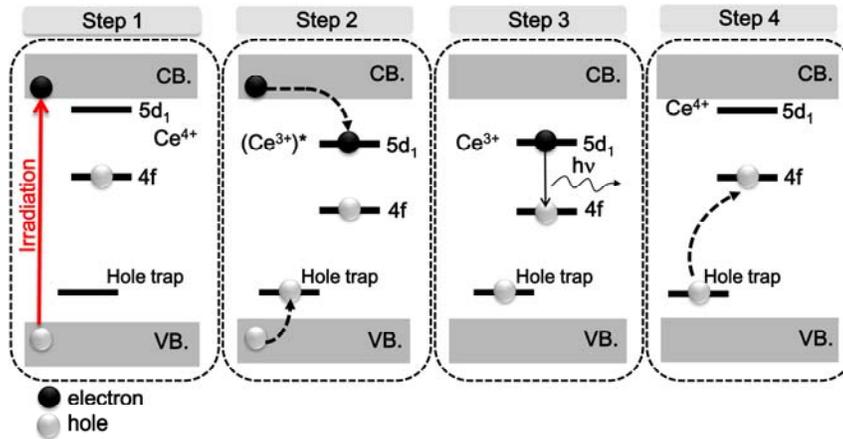
399   **FIG. 8** Schematic diagram of the role of stable Ce^{4+} in scintillation mechanism in GGAG:Ce.

400

401   **E. Applicability of the Ce^{4+} emission model**

402   As a practical demonstration, the Ce^{4+} emission model is applied to explain the improvement of

403   scintillation performance in LSO:Ce,Ca [9], LYSO:Ce,Ca/Mg [10] and LuAG:Ce,Mg [11]. For the

404   case of LuAG:Ce,Mg, the forbidden gap in LuAG is about 7.5-8.0 eV [56,57], the onset of CT is at

405   about 3.75-3.65 eV (330-340 nm) and E_{4f-5d1} is 2.79 eV (445 nm) [11]. Then, $5d_1$ should be at about 6.5

406   eV above the VB edge, which means 1-1.5 eV below the CB edge, which fits the fact that $5d_2$ level in

407   YAG was found at about 0.5 eV below CB edge [58]. The TL intensity of annealed Mg^{2+} codoped

408   LuAG:Ce is significantly reduced in comparison to that of annealed LuAG:Ce, without formation of

409   new TL peaks [11]. Thus, after Mg^{2+} codoping in LuAG:Ce, not only was the decay time accelerated

410   by the formation of Ce^{4+}, but a combination of sufficient separation between $5d_1$ state of Ce^{4+} and CB

411   (1-1.5 eV) and traps suppression both contributed to the light yield enhancement.

412   Because of the similarity between codoped LSO:Ce and codoped LYSO:Ce, either optical or

413   scintillation properties [9,12,59,60], codoped LYSO:Ce is chosen to be discussed. Using previous

414   reports on LYSO:Ce as an example, based on an E_g of 7.4 eV, an $E_{4f\text{-}5d1}$ of 3.47 eV and an E_{CT} between

415   3.54 and 3.65 eV [10], the $5d_1$ state position of Ce^{4+} is 0.28-0.39 eV below the CB. It located at a

416   higher position in the forbidden gap than the $5d_1$ of Ce^{3+} (ΔE_{ion}=0.435 eV) in LYSO:Ce [61]. Thus, the

417   formation of Ce^{4+} will result in unwanted thermal ionization effects in LYSO:Ce,Ca. Thanks to the TL

418   intensity reduction throughout the measured temperature range in Ca^{2+} codoped LYSO:Ce [14,60], trap

419   suppression and more efficient energy migration of free charge carriers to activators can be ensured,

420   which in turn in favors light yield enhancement and decay time shortening. Thus, the time response

421   optimization in Ce^{3+}-based scintillators for PET and TOF-PET applications can be achieved by

422   composition engineering through codoping ions with lower valence state and closer ionic radius with

423   respect to the substituted cations in matrix in order to increase the stable Ce^{4+} fraction, although at the

424   risk of light yield deterioration.

425

426   **IV. SUMMARY**

427   A correlation between the stable Ce^{4+} fraction and the Ca^{2+} codoping concentration has been

428   established, and we have shown that the fraction of the cerium that is in the stable Ce^{3+} state is

429   negligible in GGAG:Ce codoped with 0.4 at% Ca^{2+}. A higher position of the lowest $5d_1$ excitation state

430   of Ce^{4+} in the forbidden gap in comparison to that of Ce^{3+} was confirmed. A Ce^{4+} emission model at ns

431   scale under high-energy excitation was given through an intermediate Ce^{3+} state by capturing an

432   electron from CB, radiative de-excitation of Ce^{3+} and a return to the initial state by capturing a hole

433   from a nearby hole trap or the valence band. The underlying reasons for the decay time shortening by

434   Ca^{2+} codoping in GGAG:Ce are related to a much faster emission from Ce^{4+} in comparison to Ce^{3+} and

435   more efficient and faster energy migration of free charge carriers to activators. The deterioration of

436   light yield after Ca^{2+} codoping in GGAG:Ce is ascribed to the negative consequence of narrowed E_{cd}

437   for Ce^{4+} and formation of deep traps after Ca^{2+} codoping. An understanding of Ce^{4+} emission model is

438   essential for the composition engineering of the Ce^{3+} activated scintillators with fast timing response

439   needed for PET and TOF-PET applications. More comprehensive studies are presently under way in

440   which other material system will be studied.

441

452

453   **REFERENCES**

454   [1] S. S. Gambhir, Molecular imaging of cancer with positron emission tomography, Nat. Rev. Cancer
455   **2**, 683 (2002).

456   [2] C. L. Melcher, Scintillation crystals for PET, J. Nucl. Med. **41(6)**, 1051 (2000).

457   [3] M. J. Weber and R. R. Monchamp, Luminescence of $Bi_4Ge_3O_{12}$ - spectral and decay properties, J
458   Appl. Phys. **44**, 5495 (1973).

459   [4] C. L. Melcher and J. S. Schweitzer, Cerium-doped lutetium orthosilicate: a fast, efficient new
460   scintillator, IEEE Trans. Nucl. Sci. **39**, 502 (1992).

461   [5] D. W. Cooke, K. J. McClellan, B. L. Bennett, J. M. Roper, M. T. Whittaker, R. E. Muenchausen,
462   and R. C. Sze, Crystal growth and optical characterization of cerium-doped $Lu_{1.8}Y_{0.2}SiO_5$, J. Appl.
463   Phys. **88(12)**, 7360 (2000).

464   [6] M. Conti, State of the art and challenges of time-of-flight PET, Phys. Medica **25**, 1 (2009).

465   [7] E. Auffray, B. Frisch, F. Geraci, A. Ghezzi, S. Gundacker, H. Hillemanns, P. Jarron, T. Meyer, M.
466   Paganoni, K. Pauwels, M. Pizzichemi, and P. Lecoq, A comprehensive & systematic study of
467   coincidence time resolution and light yield using scintillators of different size, wrapping and
468   doping, IEEE Nuclear Science Symposium Conference Record, **N4-6**, 1 (2011).

469   [8] W. W. Moses, Time of flight in PET revisited, IEEE Trans. Nucl. Sci. **50(5)**, 1325 (2003).

470   [9] M. A. Spurrier, P. Szupryczynski, K. Yang, A. A. Carey, and C. L. Melcher, Effects of Ca^{2+}
471   co-doping on the scintillation properties of LSO:Ce, IEEE Trans. Nucl. Sc. **55(3)**, 1178 (2008).

472   [10] S. Blahuta, A. Bessière, B. Viana, P. Dorenbos, and V. Ouspenski, Evidence and consequences of
473   Ce^{4+} in LYSO:Ce,Ca and LYSO:Ce,Mg single crystals for medical imaging applications, IEEE
474   Trans. Nucl. Sci. **60(4)**, 3134 (2013).

475　[11] S. P. Liu, X. Q. Feng, Z. W. Zhou, M. Nikl, Y. Shi, and Y. B. Pan, Effect of Mg^{2+} co-doping on the
476　　　　scintillation performance of LuAG:Ce ceramics, Phys. Status Solidi RRL **8(1),** 105 (2014).

477　[12] M. Nikl, K. Kamada, V. Babin, J. Pejchal, K. Pilarova, E. Mihokova, A. Beitlerova, K.
478　　　　Bartosiewicz, S. Kurosawa, and A. Yoshikawa, Defect engineering in Ce-doped aluminum garnet
479　　　　single crystal scintillators, Cryst. Growth Des. DOI: 10.1021/cg501005s (2014).

480　[13] K. Yang, C. L. Melcher, M. A. Koschan, and M. Zhuravleva, Effect of Ca co-doping on the
481　　　　luminescence centers in LSO:Ce single crystals, IEEE Trans. Nucl. Sci. **58(3),** 1394 (2011).

482　[14] M. Koschan, K. Yang, M. Zhuravleva, and C. L. Melcher, A comparison of the effect of Ca^{2+}
483　　　　codoping in cerium doped GSO with that of LSO and YSO, J. Cryst. Growth **352**, 133 (2012).

484　[15] M. Nikl, J. Pejchal, E. Mihokova, J. A. Mares, H. Ogino, A. Yoshikawa, T. Fukuda, A. Vedda, and
485　　　　C. D'Ambrosio, Antisite defect-free $Lu_3(Ga_xAl_{1-x})_5O_{12}$:Pr scintillator, Appl. Phys. Lett. **88**, 141916
486　　　　(2006).

487　[16] M. Fasoli, A. Vedda, M. Nikl, C. Jiang, B. P. Uberuaga, D. A. Andersson, K. J. McClellan, and C.
488　　　　R. Stanek, Band-gap engineering for removing shallow traps in rare-earth $Lu_3Al_5O_{12}$ garnet
489　　　　scintillators using Ga^{3+} doping, Phys. Rev. B **84**, 081102(R) (2011).

490　[17] Y. T. Wu, J. L. Luo, M. Nikl, and G. H. Ren, Origin of improved scintillation efficiency in
491　　　　$(Lu,Gd)_3(Ga,Al)_5O_{12}$:Ce multicomponent garnets: An X-ray absorption near edge spectroscopy
492　　　　study, APL Mater. **2**, 012101 (2014).

493　[18] K. Kamada, T. Yanagida, J. Pejchal, M. Nikl, T. Endo, K. Tsutumi, Y. Fujimoto, A. Fukabori, and
494　　　　Y. Yoshikawa, Scintillator-oriented combinatorial search in Ce-doped $(Y,Gd)_3(Ga,Al)_5O_{12}$
495　　　　multicomponent garnet compounds, J. Phys. D: Appl. Phys. **44**, 505104 (2011).

496　[19] K. Kamada, T. Endo, K. Tsutumi, T. Yanagida, Y. Fujimoto, A. Fukabori, A. Yoshikawa, J. Pejchal,
497　　　　and M. Nikl, Composition engineering in cerium-doped $(Lu,Gd)_3(Ga,Al)_5O_{12}$ single crystal
498　　　　scintillators, Cryst. Growth Des. **11**, 4484 (2011).

499　[20] J. A. Mares, M. Nikl, E. Mihokova, A. Beitlerova, A. Vedda, and C. D'Ambrosio, Scintillation
500　　　　response comparison among Ce-doped aluminum garnets, perovskites and orthosilicate, IEEE
501　　　　Trans. Nucl. Sci. **55**, 1142 (2008).

502　[21] K. Kamada, T. Yanagida, T. Endo, K. Tsutumi, Y. Usuki, M. Nikl, Y. Fujimoto, A. Fukabori, and A.
503　　　　Yoshikawa, 2 inch diameter single crystal and scintillation properties of Ce:$Gd_3Al_2Ga_3O_{12}$, J.
504　　　　Cryst. Growth **352**, 88 (2012).

505　[22] M. Tyagi, F. Meng, M. Koschan, S. B. Donnald, H. Rothfuss, and C. L. Melcher, Effects of
506　　　　codoping on scintillation and optical properties of a Ce-doped $Gd_3Ga_3Al_2O_{12}$ scintillator, J. Phys.
507　　　　D: Applied Phys. **46**, 475302 (2013).

508　[23] F. Meng, M. Koschan, Y. T. Wu, C. L Melcher, and P. Cohen, Relationship between Ca^{2+}
509　　　　concentration and properties of GGAG:Ce scintillators, IEEE Trans. Nucl. Sci. unpublished.

510　[24] P. Dorenbos, Systematic behavior in trivalent lanthanide charge transfer energies, J. Phys.:
511　　　　Condens. Matter **15**, 8417 (2003).

512　[25] D. Z. Ding, H. Feng, G. H. Ren, M. Nikl, L. S. Qin, S. K. Pan, and F. Yang, Air atmosphere
513　　　　annealing effects on LSO:Ce crystal, IEEE Trans. Nucl. Sci. **57**, 1272 (2010).

514 [26] B. Ravel and M. Newville, ATHENA and ARTEMIS: Interactive graphical data analysis using
515   IFEFFIT, Phys. Scr. **115**, 1007 (2005).

516 [27] G. Kresse and J. Hafner, Ab initio molecular dynamics for liquid metals, Phys. Rev. B **47**, 558
517   (1993).

518 [28] G. Kresse and D. Joubert, From ultrasoft pseudopotentials to the projector augmented-wave
519   method Phys. Rev. B **59**, 1758 (1999).

520 [29] J. P. Perdew, K. Burke, and M. Ernzerhof, Generalized gradient approximation made simple, Phys.
521   Rev. Lett. **77**, 3865 (1996).

522 [30] S. L. Dudarev, G. A. Botton, S. Y. Savrasov, C. J. Humphreys, and A. P. Sutton,
523   Electron-energy-loss spectra and the structure stability of nickel oxide: An LSDA+U study, Phys.
524   Rev. B **57**, 1505 (1998).

525 [31] V. I. Anisimov, F. Aryasetiawan, and A. I. Lichtenstein, First-principles calculations of the
526   electronic structure and spectra of strongly correlated systems: the LDA+U method, J. Phys.:
527   Condens. Matter **9**, 767 (1997).

528 [32] Y. N. Xu, W. Y. Ching, and B. K. Brickeen, Electronic structure and bonding in garnet crystals
529     $Gd_3Sc_2Ga_3O_{12}$, $Gd_3Sc_2Al_3O_{12}$, and $Gd_3Ga_5O_{12}$ compared to $Y_3Al_5O_{12}$, Phys. Rev. B **61**, 1817
530   (2000).

531 [33] J. P. Perdew, M. Ernzerhof, and K. Burke, Rationale for mixing exact exchange with density
532   functional approximations, Chem. Phys. **105**, 9982 (1996).

533 [34] L. Hedin, New method for calculating the one-particle green's function with application to the
534   electron-gas problem, Phys. Rev. **139**, A796 (1965).

535 [35] Y. N. Xu and W. Y. Ching, Electronic structure of yttrium aluminum garnet ($Y_3Al_5O_{12}$), Phys. Rev.
536   B **59**, 10530 (1999).

537 [36] A. Zunger, S.-H. Wei, L. G. Ferreira, and J. E. Bernard, Special quasirandom structures, Phys. Rev.
538   Lett. **65**, 353 (1990).

539 [37] See Supplemental Materials at [] for crystal data and structure refinement for $Gd_3Ga_3Al_2O_{12}$.

540 [38] Y. T. Wu, M. Nikl, V. Jary, and G. H. Ren, Thermally induced ionization of $5d_1$ state of Ce^{3+} ion in
541     $Gd_3Ga_3Al_2O_{12}$ host, Chem. Phys. Lett. **574**, 56 (2013).

542 [39] W. Chewpraditkul, C. Wanarak, T. Szczesniak, M. Moszynski, V. Jary, A. Beitlerova, and M. Nikl,
543   Opt. Mater. **35(9)**, 1679 (2013).

544 [40] J. A. Dean, Lange's handbook of chemistry, (15th edition) McGraw-Hill, New York (1979).

545 [41] C. Mansuy, J. M. Nedelec, and R. Mahiou, Molecular design of inorganic scintillators: from
546   alkoxides to scintillating materials, J. Mater. Chem. **14**, 3274 (2004).

547 [42] C. L. Melcher, S. Friedrich, S. P. Cramer, M. A. Spurrier, P. Szupryczynski, and R. Nutt, Cerium
548   oxidation state in LSO:Ce scintillators, IEEE Trans. Nucl. Sci. **52(5)**, 1809 (2005).

549 [43] M. Fasoli, A. Vedda, A. Lauria, F. Moretti, E. Rizzelli, N. Chiodini, F. Meinardi, and M. Nikl,
550   Effect of reducing sintering atmosphere on Ce-doped sol-gel silica glasses, J. Non-Cryst. Solids
551   **355**, 1140 (2009).

552 [44] P. Dorenbos, Electronic structure and optical properties of the lanthanide activated
553     $RE_3(Al_{1-x}Ga_x)_5O_{12}$ (RE=Gd,Y, Lu) garnet compounds, J. Lumin. **134**, 310 (2013).

554 [45] C. R. Stanek, C. Jiang, S. K. Yadav, K. J. McClellan, B. P. Uberuaga, D. A. Andersson, and M.
555   Nikl, The effect of Ga-doping on the defect chemistry of $RE_3Al_5O_{12}$ garnets, Phys. Status Solidi (b)
556   **250**, 244 (2013).

557 [46] A. Belén Muñoz-García and L. Seijo, Structural, electronic, and spectroscopic effects of Ga
558   codoping on Ce-doped yttrium aluminum garnet: First-principles study, Phys. Rev. B **82**, 184118
559   (2010).

560 [47] Y. Zorenko, T. Zorenko, T. Voznyak, Luminescence centers in $Y_3Al_5O_{12}$:La single crystals, J.
561   Phys.: Conf. Ser. **289**, 012028 (2011).

562 [48] V. Babin, V. V. Laguta, A. Maaroos, A. Makhov, M. Nikl, and S. Zazubovich, Luminescence of
563   F^+-type centers in undoped $Lu_3Al_5O_{12}$ single crystals, Phys. Status Solidi (b) **248**, 239 (2011).

564 [49] L. Guerbous and O. Krachni, Luminescence of Ce^{3+} traces in Pr^{3+}-doped $LuBO_3$ and YBO_3
565   orthoborates, Radiat. Eff. Defect Solid. **161**, 199 (2006).

566 [50] P. A. Tanner, C. S. K. Mak, N. M. Edelstein, K. M. Murdoch, G. Liu, J. Huang, L. Seijo, and Z.
567   Barandiarán, Absorption and emission spectra of Ce^{3+} in elpasolite lattices, J. Am. Chem. Soc.
568   **125**, 13225 (2003).

569 [51] L. Van Pieterson, S. Soverna, and A. Meijerink, On the nature of the luminescence of Sr_2CeO_4, J.
570   Electrochem. Soc. **147(12)**, 4688 (2000).

571 [52] L. Li, S. Zhou, and S. Zhang, Investigation on charge transfer of Ce^{4+} in Sr_2CeO_4 blue phosphor,
572   Chem. Phys. Lett. **453**, 283 (2008).

573 [53] S. R. Rotman, H. L. Tuller, and C. Warde, Defect-property correlations in garnet crystals. VI. The
574   electrical conductivity, defect structure, and optical properties of luminescent calcium and
575   cerium-doped yttrium aluminate garnet, J. Appl. Phys. **71**, 1209 (1992).

576 [54] B. Liu, C. S. Shi, Y. G. Wei, and J. Y. Liao, the traps effect on temperature dependence of
577   luminescence from $PbWO_4$ crystals, Chem. Phys. Lett. **362**, 296 (2002).

578 [55] A.J. Wojtowicz, A. Lempicki, D. Wisniewski, M. Balcerzyk, and C. Brecher, The carrier capture
579   and recombination processes in Ln^{3+}-activated scintillators, IEEE Trans. Nucl. Sci. **43**, 2168
580   (1996).

581 [56] V. Babin, K. Blazek, A. Krasnikov, K. Nejezchleb, M. Nikl, T. Savikhina, and S. Zazubovich,
582   Luminescence of undoped LuAG and YAG crystals, Phys. Stat. Sol. (c) **2(1)**, 97 (2005).

583 [57] M. Kirm, A. Lushchik, Ch. Lushchik, and G. Zimmerer, in: Physics and Chemistry of Luminescent
584   Materials, edited by C. Ronda et al., The Electrochem. Soc. Proc. Ser. PV 99-40 (The
585   Electrochemical Society, Pennington, NJ, 113-122 (2000).

586 [58] D.S. Hamilton, S.K. Gayen, G.J. Pogatshnik, R.D. Ghen, and W.J. Miniscalco, Optical-absorption
587   and photoionization measurements from the excited states of Ce^{3+}:$Y_3Al_5O_{12}$, Phys. Rev. B **39(13)**,
588   8807 (1989).

589 [59] B. Ferrand, B. Viana, L. Pidol, and P. Dorenbos, Low-delayed luminescence dense and rapid
590   scintillator material, U.S. Patent, No. 7,651,632 B2 (2010).

591 [60] B. Ferrand, B. Viana, L. Pidol, and P. Dorenbos, Dense high-speed scintillator material of low
592   afterglow, U.S. Patent 8,034,258 B2 (2010).

593 [61] H. Feng, V. Jary, E. Mihokova, D. Z. Ding, M. Nikl, G. H. Ren, H. Y. Li, S. K. Pan, A. Beitlerova,

21

594   and R. Kucerkova, Temperature dependence of luminescence characteristics of

595    $Lu_{2(1-x)}Y_{2x}SiO_5$:Ce^{3+} scintillator grown by the Czochralski method, J. Appl. Phys. **108**, 033519

596   (2010).